

Influence of biomass burning on mixing state of sub-micron aerosol particles in the North China Plain



Simonas Kecorius^a, Nan Ma^{a, c, *}, Monique Teich^a, Dominik van Pinxteren^a, Shenglan Zhang^d, Johannes Größ^a, Gerald Spindler^a, Konrad Müller^a, Yoshiteru Iinuma^a, Min Hu^b, Hartmut Herrmann^a, Alfred Wiedensohler^a

^a Leibniz-Institute for Tropospheric Research, Permoserstr. 15, Leipzig, Germany

^b College of Environmental Sciences and Engineering, Peking University, Beijing 100871, China

^c Multiphase Chemistry Department, Max Planck Institute for Chemistry, Mainz 55128, Germany

^d Chengdu University of Information Technology, Chengdu 610225, China

HIGHLIGHTS

- Biomass burning aerosol particles are moderately volatile and mixed internally.
- Particle hygroscopicity did not change during biomass burning.
- Single scattering albedo is sensitive to particle mixing state especially during biomass burning.

ARTICLE INFO

Article history:

Received 20 November 2016

Received in revised form

25 March 2017

Accepted 16 May 2017

Available online 17 May 2017

Keywords:

Biomass burning

Sub-micron aerosol particles

Mixing state

ABSTRACT

Particulate emissions from crop residue burning decrease the air quality as well as influence aerosol radiative properties on a regional scale. The North China Plain (NCP) is known for the large scale biomass burning (BB) of field residues, which often results in heavy haze pollution episodes across the region. We have been able to capture a unique BB episode during the international CAREBeijing-NCP intensive field campaign in Wangdu in the NCP (38.6°N, 115.2°E) from June to July 2014. It was found that aerosol particles originating from this BB event showed a significantly different mixing state compared with clean and non-BB pollution episodes. BB originated particles showed a narrower probability density function (PDF) of shrink factor (SF). And the maximum was found at shrink factor of 0.6, which is higher than in other episodes. The non-volatile particle number fraction during the BB episode decreased to 3% and was the lowest measured value compared to all other predefined episodes. To evaluate the influence of particle mixing state on aerosol single scattering albedo (SSA), SSA at different RHs was simulated using the measured aerosol physical-chemical properties. The differences between the calculated SSA for biomass burning, clean and pollution episodes are significant, meaning that the variation of SSA in different pollution conditions needs to be considered in the evaluation of aerosol direct radiative effects in the NCP. And the calculated SSA was found to be quite sensitive on the mixing state of BC, especially at low-RH condition. The simulated SSA was also compared with the measured values. For all the three predefined episodes, the measured SSA are very close to the calculated ones with assumed mixing states of homogeneously internal and core-shell internal mixing, indicating that both of the conception models are appropriate for the calculation of ambient SSA in the NCP.

© 2017 The Author(s). Published by Elsevier Ltd. This is an open access article under the CC BY-NC-ND license (<http://creativecommons.org/licenses/by-nc-nd/4.0/>).

1. Introduction

Biomass burning (BB) is one of the major sources of atmospheric carbonaceous aerosol particles. During BB processes, high quantities of organic compounds, elemental carbon, carbon monoxide and carbon dioxide gas, mercury and other pollutants are emitted

* Corresponding author. Leibniz-Institute for Tropospheric Research, Permoserstr. 15, Leipzig, Germany.

E-mail address: ma@tropos.de (N. Ma).

to the atmosphere (e.g. Andreae and Merlet, 2001; Pirrone et al., 2010). BB is known to have effects on regional air quality and climate. For example, a significant relation between childhood asthma admissions and increase in particulate matter (PM) from BB was showed by Nastos et al. (2010). Transported to remote areas, BB products can cause the exceedances of predetermined particulate matter limits, decreased visibility and the degradation of air quality (e.g. Jaffe et al., 2003; Jacob et al., 2003). Aerosol generated in BB may also have a large radiative forcing on regional scales (Christopher et al., 1996; Hobbs et al., 1997). Its radiative forcing is found to be strongly influenced by its aging state (e.g. Zhuang et al., 2013; Chung et al., 2012; Jacobson, 2001).

Worldwide, chemical composition and mixing state of BB aerosol were the subjects in numerous studies. Pratt et al. (2011) found that in fresh BB plume the average mass fraction of particles was dominated by organics (80–90%), followed by soot (0.3–13%), nitrate (1–3%), chloride (0.8–2%), sulfate (0–1%) and ammonium (0.2–0.4%). In another study (Reid et al., 2005), inorganic salts were found to account for 12–15% of fresh smoke particles. Non-volatile water-insoluble organic polymers, to some extent similar to high-molecular weight humic-like substances (HULIS) were also reported to be products of BB (Pósfai et al., 2004; Tivanski et al., 2007). These substances are known as the tar balls (TB). Recent laboratory studies also suggest that TBs are produced by the ejection of liquid tar droplets during the biomass burning, which then dominate the number fraction of BB particles in a size range from 100 to 600 nm (Tóth et al., 2014).

A recent study in Germany using Weather Research and Forecast (WRF) model showed that the particle light absorption coefficient can be biased by 20% (Nordmann et al., 2014). The treatment of the state of mixing (external versus internal) of black carbon (BC) in the WRF was underlined as a potential cause for miscalculation of optical properties. The importance of the state of mixing of aerosol particles was also addressed in regional climate and chemistry modeling system RegCCMS (Zhuang et al., 2013). It was shown that the mixing state and hygroscopicity of carbonaceous aerosol particle determine aerosol direct radiative forcing and corresponding climate responses.

In China, aerosol particle mixing state during biomass burning was also addressed by several studies. Bi et al. (2011) found that in the Pearl River Delta region, as much as 90% of the particles were mixed internally together with some secondary inorganic species. K-Na-rich substances were observed in 12% of the particles. The fractions of nitrate and particulate sulfate in particles in the accumulation size range were by 10% higher than in non-BB related pollution episodes. A study in the Guanzhong Plain, Xi'an, showed that during polluted episodes about 49% of the refractory BC was internally mixed with non-refractory materials, which is 27% higher than in clean periods (Wang et al., 2014). Organics were suggested to be a primary contributor to BC coating, which was found to enhance light absorption by a factor of 1.8. Lan et al. (2013) investigated the influence of BC mixing state on its mass absorption efficiency (MAE) in south China. The percentage of internally mixed BC was found to be 24%, amplifying MAE by 7%.

To our knowledge, studies on the mixing state of aerosol particle properties, during BB events, specifically in the NCP are still scarce. This limitation may significantly contribute to the uncertainties in the evaluation of aerosol radiative forcing, especially in the North China Plain (NCP), where most of China's agricultural fires are registered. The NCP, covering an area of about 410 000 square kilometers, is the area where up to 50% of annual China demand of cotton and cereal is produced (Godfray et al., 2010). It is also the major region for wheat, meaning that harvest seasons usually starts in June, after which BB activities start to spread from south to north (Ni et al., 2015). It leads to a regional degradation of air quality and

accelerate the climatic change over East Asia (Zheng et al., 2005; Cheng et al., 2013; Jeong et al., 2014).

Recent assessments of aerosol radiative effects have highlighted the need for better spatial coverage of BC mass concentration, mixing state and optical properties, which are crucial for reducing the uncertainties in radiative forcing evaluation and improving pollution control strategies. In this study, we have applied the state of art instrumentation coupled with offline chemical analysis to investigate the mixing state of BB aerosol particles and the resulting aerosol optical properties in the NCP.

2. Experimental

2.1. Measurement site

The measurements were conducted at a rural site in the NCP (38.6°N 115.2°E, shown as the black square in Fig. 3A), around 5 km south-east of Wangdu town and 170 km south-west of Beijing. Such a site is the best choice for investigating the well-mixed regional air pollution of the NCP as there were no industrial or residential activities in the vicinity of the station. The measurement containers were located in an open field surrounded by farmland. The nearest living areas and the roads were about 2 and 1 km away from the measurement site, respectively. The aerosol instruments were placed in an air-conditioned (24 °C) TROPOS mobile laboratory. The sampling line consists of a PM₁₀ inlet (16.67 l min⁻¹, 6 m above ground level), followed by two 1.5 m Nafion dryers and an automatic drying chamber, in which the relative humidity (RH) of aerosol sample was regulated to be below 30% (Tuch et al., 2009). The aerosol sample was directed to the instruments via an isokinetic flow splitter and stainless steel/conductive rubber tubing.

2.2. Volatility tandem differential mobility analyzer (V-TDMA)

In this study, a TROPOS-type V-TDMA system (Philippin et al., 2004) was used to determine the mixing state of aerosol particles in terms of volatility. The refractory fractions of aerosol particles with certain sizes (20, 30, 50, 100, 150 and 250 nm) were retrieved by evaporating the volatile material in a thermal conditioning column at 300 °C. V-TDMA scans at 25 °C were used to calibrate the kernel function (Gysel et al., 2009). Particle transport efficiency was measured using generated NaCl particles under laboratory conditions. The time resolution of the measurement was adjusted to be less than 1 h.

In this study, species which did not evaporate at 300 °C were referred as refractory. TDMAinv routine (Gysel et al., 2009) was used to retrieve the Probability Density Function of shrink factor (SF-PDF). The shrink factor is defined as $SF = \frac{D_{300}}{D_{25}}$, where D_{25} and D_{300} are respectively particle diameters at 25 °C and 300 °C. SF-PDFs were integrated within the ranges of $SF > 0.85$, $0.5 < SF < 0.85$ and $SF < 0.5$ to retrieve number fractions of non-volatile (NV), semi volatile (SV) and highly volatile (HV) particles, respectively. We have also used a term “externally mixed” further in the paper, which refers to the fraction of NV particles. Furthermore, an assumption that all particles contain a non-volatile core has been made. In general, this assumption leads to an over-estimation of the refractory fraction because of two reasons. Firstly, heated aerosol particles may shrink to sizes below the detection limit (10 nm) of the condensation particle counter (CPC). Secondly, the number fraction of completely volatile particles usually does not exceed 10–20%, but might be as high as 60% during new particle formation events (Wehner et al., 2009). The authors are aware of these possible sources of uncertainties and the needed precautions were made in data evaluation process and discussion of the results. The volume fraction remaining (VFR) of aerosol

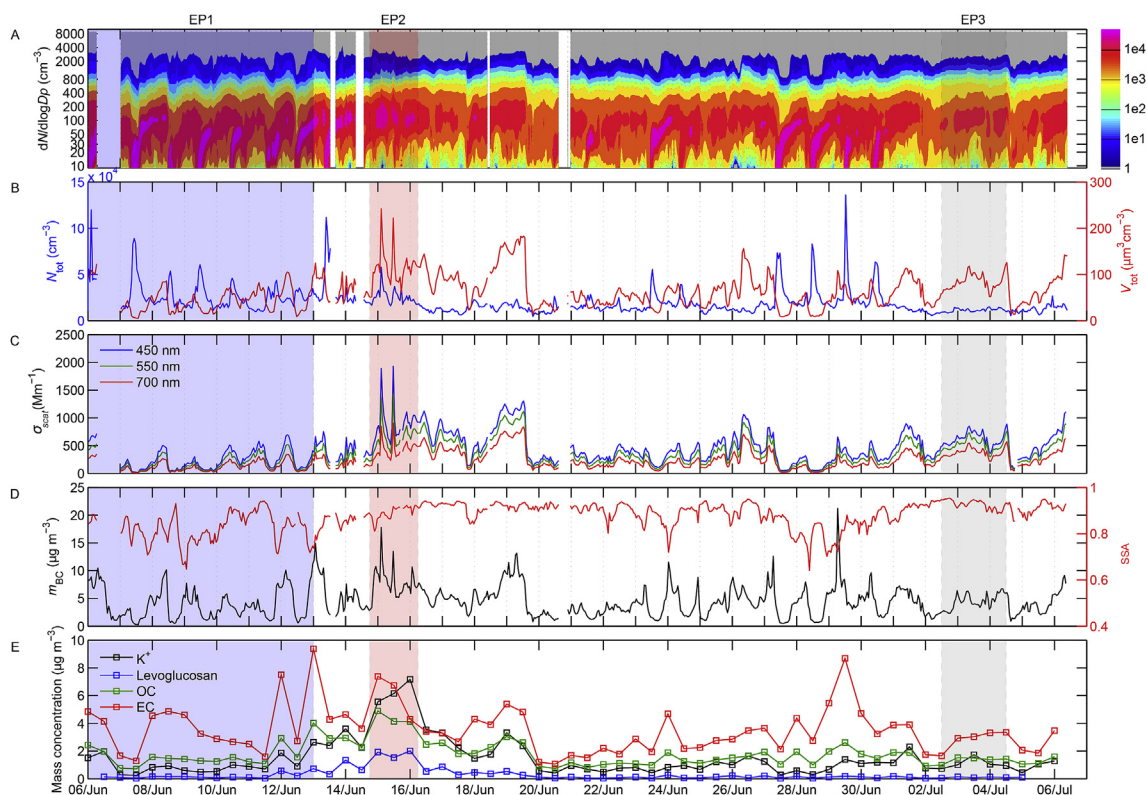


Fig. 1. Time series of (A) aerosol particle number size distribution, (B) particle number (N_{tot}) and volume concentration (V_{tot}), (C) aerosol scattering coefficients (σ_{scat}) at 3 wavelengths, (D) black carbon mass concentration and single scattering albedo (SSA) at wavelength of 637 nm, and (E) offline chemical analysis of K^+ , levoglucosan, OC and EC. Blue, red and gray color shades mark the clean episode (EP1), BB episode (EP2) and pollution episode (EP3), respectively.

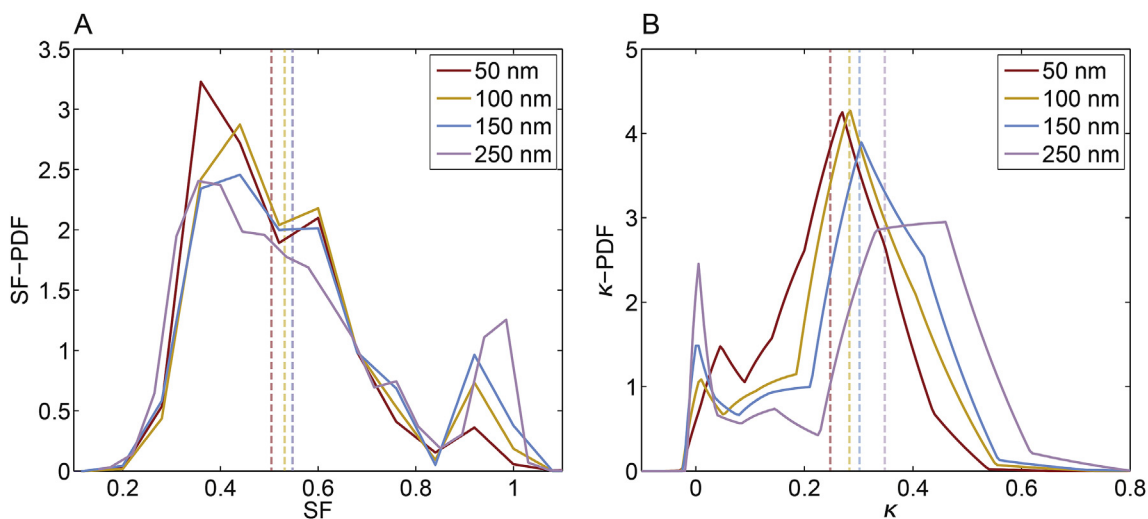


Fig. 2. Campaign-averaged probability density functions (PDF) of shrink factor (A) and κ (B), the dashed lines show the arithmetic mean values.

particles after heating was extracted from TDMAinv routine as explained by Gysel et al. (2009).

2.3. High humidity tandem differential mobility analyzer (HH-TDMA)

Size-resolved hygroscopic growth factor (GF) of ambient aerosol particles at high RH was measured using a TROPOS HH-TDMA (Hennig et al., 2005; Liu et al., 2011). Particle hygroscopic growth

factor is defined as $GF = \frac{D_{RH}}{D_{dry}}$, where D_{dry} and D_{RH} are respectively particle diameters at dry condition and after being humidified. The main difference between the conventional H-TDMA (Rader and McMurry, 1986) and the high humidity system lays in the temperature stability and humidification of the aerosol/sheath air. Temperature fluctuations in the second differential mobility analyzer (DMA) cause instabilities in RH, making measurements at RHs above 90% nearly impossible with conventional systems. In HH-TDMA, two separate water baths are used to control the

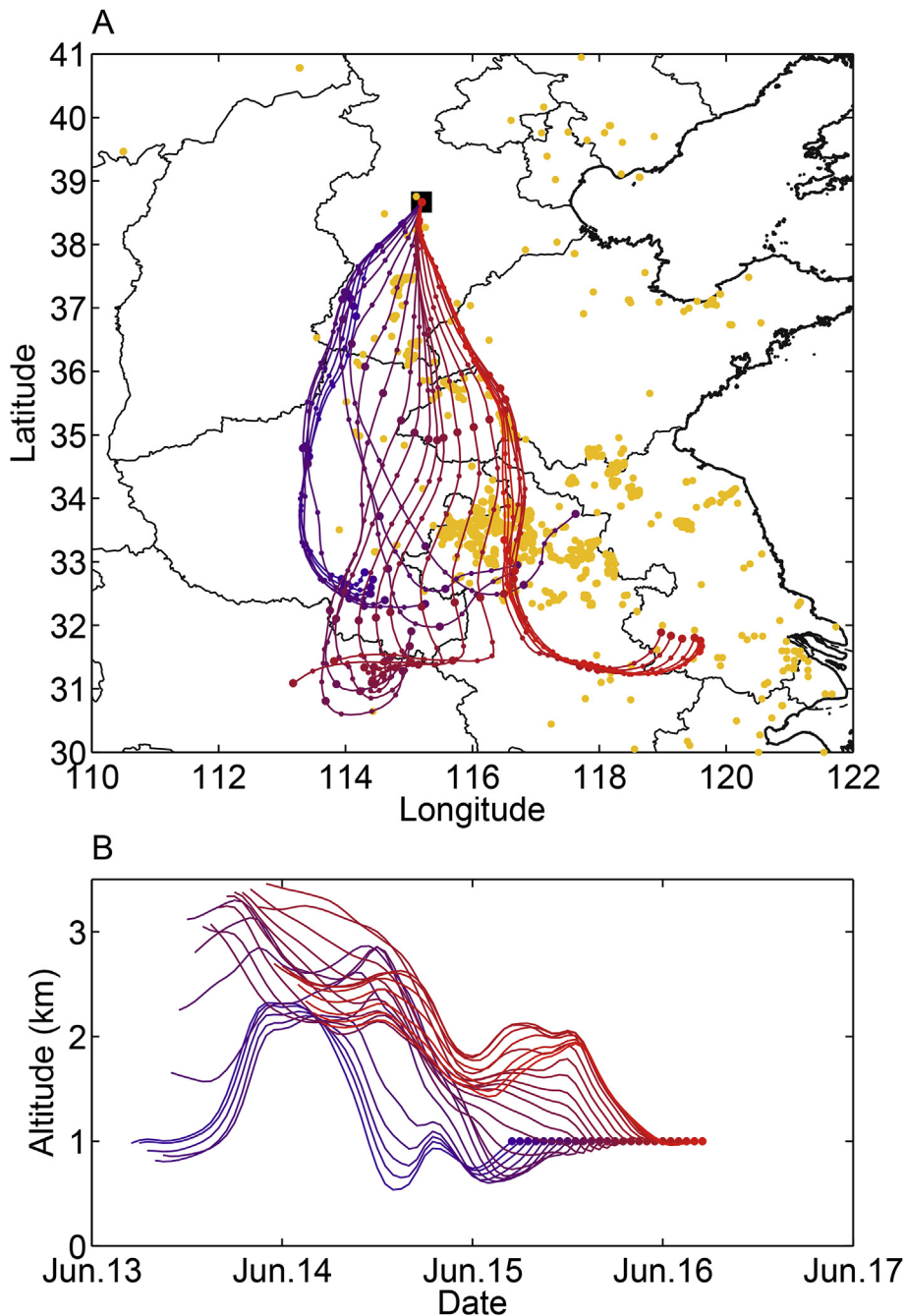


Fig. 3. (A) Fire spots (yellow dots) during June 12–14, 2014 from FIRMS and 48-h backward trajectories (colored lines). The colors of the lines show their different arriving time. On each backward trajectory, the time interval between two small dots is 3 h, and between two big dots it is 12 h. (B) Time series of altitude of the backward trajectories.

temperature of both the humidity conditioning section and the second DMA which are immersed in water. Temperature is maintained within ± 0.1 K with a stability of ± 0.02 K. This ensures that RH in the second DMA can reach 98% with $\pm 1.2\%$ accuracy. To calibrate the RH in HH-TDMA system, the GFs of ammonium sulfate particles of 100 nm dry diameter were measured every day at 17:00 LT. During the measurement campaign the dry initial diameters selected by the first DMA were set to 30, 50, 100, 150, 200, 250 nm and 98% RH was chosen in the second DMA. The time resolution of the system was adjusted to be approximately 1 h.

TDMAinv routine by Gysel et al. (2009) was used to retrieve the Probability Density Functions of GF (GF-PDF). To get rid of the

curvature effect and facilitate the comparison of hygroscopicity of particles with different diameters, hygroscopicity parameter κ is calculated (Petters and Kreidenweis, 2007):

$$\kappa(GF) = (GF^3 - 1) \cdot \left[\frac{1}{S} \exp\left(\frac{4\sigma_{s/a}M_W}{RT\rho_W D_d GF}\right) - 1 \right]$$

Where S is saturation ratio; ρ_W is water density; M_W is the molecular weight of water; $\sigma_{s/a}$ is the surface tension of the solution/air interface which is assumed to be the same as the surface tension of the pure water/air interface; R is the universal gas constant; T is the temperature. The probability density functions of κ (κ -PDFs) were integrated between three ranges to get the number

fractions of nearly hydrophobic (NH, $\kappa < 0.1$), slightly hygroscopic (SH, $0.1 \leq \kappa < 0.2$) and more hygroscopic (MH, $\kappa \geq 0.2$) particles.

2.4. Particle number size distribution measurements

Dry-state (RH below 30%) particle number size distributions (PNSD) in a mobility size range from 3 to 800 nm were recorded using a TROPOS-type dual mobility particle size spectrometer (MPSS). The detailed principles of the custom built closed loop TROPOS MPSS is described in Wiedensohler et al. (2012). Recorded particle mobility distributions were inverted to PNSD using the algorithm developed by Pfeifer et al. (2014). The time resolution of the measurement is 10 min. Corrections for transmission losses in the sampling lines and CPC counting efficiency were also applied to the data (Wiedensohler et al., 1997).

Polystyrene latex spheres (PSL, Thermo Scientific, Duke Standards) of 203 nm were used to check the sizing accuracy of the DMAs. And the high voltage supply offset calibrations were performed regularly on all DMA based instruments. Instrument flow checks (using primary standard airflow calibrator) and zero checks for all instruments were performed on a weekly basis. On average deviations in the sample flow did not exceed 1.5% for all instruments throughout the measurement campaign.

2.5. Particle light absorption measurements

A multi-angle absorption photometer (MAAP Model 5012, Thermo, Inc., Waltham, MA USA; Petzold and Schönlinner, 2004) was used to quantify the particle light absorption coefficient at a wavelength of 637 nm. The instrument operates by converting the light attenuation into an absorption coefficient. Backscattering of the filter is included in radiative transfer calculation for a higher accuracy. The MAAP flow was adjusted to 3 L min^{-1} using a custom made nozzle to save filter material. The temporal resolution of the measurement was set to 1 min. The MAAP may suffer from an artifact after a filter spot change at high absorption coefficient (Hyvärinen et al., 2013). This artifact was visible in our measurement, and the influenced data was removed from the time series.

2.6. Particle light scattering measurements

Aerosol light scattering and hemispheric backscattering coefficient were measured at wavelengths of 450, 550 and 700 nm with an integrating nephelometer (Model 3563, TSI, Inc., Shoreview, MN USA; Heintzenberg and Charlson, 1996; Anderson et al., 1996). The temporal resolution of the measurement was 1 min. The nephelometer was regularly calibrated using CO_2 . And the calibration constants stayed within 5% during the campaign period. Checks with particle-free zero air were performed four times per day.

2.7. Aerosol chemical measurements

For an offline filter analysis, PM_{10} aerosol particles ($< 10 \mu\text{m}$) were collected on quartz fiber filters using a high volume sampler. Samples were taken with 12 h time resolution (day: 06:00–18:00 LT, night: 18:00–06:00 LT) at a flow rate of $0.5 \text{ m}^3 \text{ min}^{-1}$. The filters were pre-heated at $105 \text{ }^\circ\text{C}$ for 24 h before usage. Aerosol loaded filters were stored at $-20 \text{ }^\circ\text{C}$ until analysis. A portion of the sampled filter (9.42 cm^2) was extracted and dissolved into 20 mL of ultra-pure water by shaking with a laboratory orbital shaker for 120 min. An aliquot of the solution was analyzed for levoglucosan, mannosan and galactosan as described by Iinuma et al. (2009). Another aliquot was analyzed for inorganic ions (K^+ , Na^+ , NH_4^+ , Mg^+ , Ca^{2+} , Cl^- , NO_3^- , SO_4^{2-} , NO_2^-) by ion chromatography (IC690 Metrohm, Switzerland; ICS3000, Dionex, USA). Organic and elemental carbon

(OC and EC) were determined following the EUSAAR 2 protocol (Cavalli et al., 2010). The uncertainties for this method are estimated to be below 10%.

2.8. Backward trajectories and FIRMS fire information

Information from the Fire Information for Resource Management System (FIRMS) operated by National Aeronautics and Space Administration (NASA) of the United States (available at <https://earthdata.nasa.gov/data/near-real-time-data/firms>, accessed 26 November 2015) was used to identify the possible biomass burning regions. The Hybrid Single-Particle Lagrangian Integrated Trajectory (HYSPLIT4) model was used to check particulate matter pathways to the measurement site (Draxler and Rolph, 2013). 48-hour backward trajectories starting at 1 km above ground level were calculated using Global Data Assimilation System meteorological data (Rolph, 2013).

3. Results and discussion

3.1. Overview of the measurement

During the intensive measuring period from June 6 to July 6, 2014, particle number size distribution, light absorption and scattering coefficients, chemical composition, and mixing state in terms of hygroscopicity and volatility were continuously measured at our station in Wangdu. The temporal variations of measured parameters are shown in Fig. 1 and a statistical summary of the data is presented in Table 1.

The arithmetic mean and standard deviation of the particle light absorption coefficient (σ_{abs}), as well as total aerosol particle volume (V_{tot}) and number concentrations (N_{tot}) during the measurement period were $31 \pm 19 \text{ Mm}^{-1}$, $63 \pm 37 \mu\text{m}^3 \text{ cm}^{-3}$, and $20\,200 \pm 15\,100 \text{ cm}^{-3}$, respectively. The scattering coefficient (σ_{scat}) at the wavelengths of 450, 550 and 700 nm were 442 ± 288 , 345 ± 235 and $236 \pm 168 \text{ Mm}^{-1}$, respectively. Offline analysis of PM_{10} high volume sampler filters showed that campaign average OC and EC mass concentrations were 17.8 ± 8.9 and $3.6 \pm 1.7 \mu\text{g m}^{-3}$, respectively. These results are comparable with previous studies conducted in the NCP (e.g. Ma et al., 2011; Zhang et al., 2016). A clean episode with pronounced new particle formation events (EP1) and two pollution episodes (EP2 and EP3) are selected (marked as colored shades in Fig. 1) and will be discussed more in detail in Sect. 3.3.

Campaign-averaged probability density functions of shrink factor and hygroscopicity parameter κ for different particle sizes are presented in Fig. 2. The integrated number fractions of particles with different volatility and hygroscopicity are list in Table 2. It can be seen that both SF-PDFs and κ -PDFs exhibit a clear bi-modal shape.

The number fraction of NV particles increases from 4 to 13% with the particle diameter increasing from 50 to 250 nm. This phenomenon was also observed in previous studies and was assigned to locally emitted BC (Wehner et al., 2009; Zhang et al., 2016). The highest number fraction of 55% of HV particles was registered in the smallest measured particle size. The number fraction of HV particles in the diameter range from 100 to 250 nm was around 49%.

The highest NH particle number fraction of 12% was observed in 50 nm size range. It can also be seen in Fig. 2B that the NH mode of 50 nm particles is slightly shifted towards higher κ values. The number fraction of hydrophobic particles with $\kappa = 0$ gradually decreased with a decreasing particle size. This observation was consistent with particle volatility, where NV particle number fraction increased with increasing particle size. The highest number fraction of MH particles was observed at 250 nm where the MH

mode is centered at κ of 0.4. The arithmetic mean of κ -PDF shifted towards higher κ values with increasing particle size (Fig. 2B). In general, accumulation mode particles were found to be mixed internally more than sub 100 nm particles. This is a result of atmospheric aging, during which aerosol particles become more volatile and hygroscopic (Liu et al., 2011; Zhang et al., 2016).

3.2. Biomass burning event

An intensive BB episode was observed on 14 to 16 of June 2014 (Fig. 1A, EP2). Time variation of the anhydrosugar levoglucosan (1,6-anhydro-D-glucopyranose) and water soluble potassium (K^+), commonly taken as tracers for BB (Zhang et al., 2013; Simoneit et al., 1999), are shown in Fig. 1E. A noticeable increase in mass concentration of levoglucosan and K^+ can be seen on 14 to 16 of June, with maximum values of 2012 ng m^{-3} and $7.2 \text{ } \mu\text{g m}^{-3}$, respectively. These values were much higher than the mean concentrations during the whole measurement period ($290 \pm 420 \text{ ng m}^{-3}$ and $1.5 \pm 1.6 \text{ } \mu\text{g m}^{-3}$). Such increases in mass concentration of levoglucosan and K^+ prove that during these days the dominant aerosol particles have originated from biomass burning. Other physical-chemical measures, such as σ_{abs} , σ_{scat} , V_{tot} , OC and EC mass concentrations, were also almost 2 times higher than their campaign averaged values.

Comparing to other BB-related studies, our observed mass concentration of levoglucosan and K^+ were considerably higher. Cheng et al. (2013) reported average ambient levoglucosan and K^+ mass concentrations in summer in Beijing to be $230 \pm 370 \text{ ng m}^{-3}$ and $1.7 \pm 2.3 \text{ } \mu\text{g m}^{-3}$, respectively. In the same study, the BB episode was characterized by $750 \pm 680 \text{ ng m}^{-3}$ of levoglucosan and $5.8 \pm 2.7 \text{ } \mu\text{g m}^{-3}$ of K^+ . However, it is worth noting that in the study by Cheng et al. (2013) the aerosol was sampled through a $\text{PM}_{2.5}$ inlet, which might have caused underestimates due to different particle cut-off size.

Satellite images of fire spots from FIRMS were analyzed to determine the region where BB did occur. It can be seen from Fig. 3A that the highest density of fire spots were registered in the regions which are known to be a major producers of wheat. The fires of crop residues start to spread in this region at the end of harvest season – June. Air mass backward trajectories of 48 h (Fig. 3) identified that BB products were transported from the biomass burning region to our measurement station and resulted in a high observed aerosol loading.

3.3. Mixing state of aerosol particles

As highlighted previously, only limited amount of studies of particle mixing state during BB are available for the NCP. In this section we will present particle mixing state in terms of hygroscopicity and volatility during a BB episode (EP2), based on in-situ

HH-TDMA and V-TDMA measurements. As a reference, particle mixing state during a clean episode (EP1) and a non-BB related pollution episode (EP3) will be firstly overviewed in section 3.3.1. The mixing state of BB particles and its differences from non-BB episodes will be discussed then in a section 3.3.2. All selected episodes are shown in Fig. 1.

3.3.1. Particle mixing state during clean and non-BB related pollution episodes

An episode with low aerosol particle loading, EP1, during which σ_{abs} , σ_{scat} and V_{tot} were lower than the overall campaign average, was chosen as a clean episode. During this episode, the mixing state of ultrafine particles is mainly determined by new particle formation (NPF). NPF with a subsequent growth was observed on 52% of the campaign days with air masses prevailing from north, which are known to favor NPF (Wu et al., 2007; Wehner et al., 2008). In previous studies, the growth of nucleation mode particles in China was assigned to secondary produced ammonium sulfate (Wiedensohler et al., 2009; Yue et al., 2010). As a result, the number fraction of HV particles increased to 67% in EP1. Newly formed and slightly grown particles had the lowest VFR and were highly volatile. As shown in Fig. 5A, a clear diurnal pattern in VFR shows that the minimum value, about 5%, of VFR was observed during noon when the NPF was most prominent. Despite high volatility of newly formed particles, non-refractory cores still existed. This might be the result of certain organic components produced in NPF in the NCP (Kecorius et al., 2015). In previous studies it was shown that the non-BC refractory fraction in newly formed particles is possibly formed of non-volatile oligomers, organic salts and polymers (Birmili et al., 2010; Ehn et al., 2014). A clear diurnal variation in VFR was also observed for 100–150 nm diameter particles in EP1. The higher level of VFR during nighttime can be explained by a shallower planetary boundary layer and higher local emission.

Another distinct property of aerosol particles in EP1 was their broad SF-PDF (Fig. 4A–D). During the clean episode, the particles might consist of background aerosol, locally freshly emitted aerosol and secondary formed aerosol etc., and none of them dominates the aerosol mass, which is different from the case in BB and polluted episodes. Particles from different originations might have different volatility. Therefore, a broad distribution of shrink factors was observed in the clean episode.

We have also captured a non-BB related pollution episode (EP3 in Fig. 1), which is defined as a period with V_{tot} stays within the top 20% highest values for at least 48 h. During this episode, we observed explicitly different particle volatility and hygroscopicity behaviors compared to EP1. As can be seen from volatility distributions in Fig. 4, highly volatile particles with a narrower HV mode dominated the SF-PDF in EP3. Particle VFR varied between 10 and 30% with a clear diurnal pattern and was in the similar range as in EP1, as shown in Fig. 5. However, different from EP1 of which VFR

Table 1
Summary of aerosol particle physical-chemical parameters (average \pm standard deviation).

Date 2014-	$\sigma_{abs637}, \text{Mm}^{-1}$	$\sigma_{scat450}, \text{Mm}^{-1}$	$\sigma_{scat550}, \text{Mm}^{-1}$	$\sigma_{scat700}, \text{Mm}^{-1}$	$N_{tot}, \text{cm}^{-3} \cdot 10^4$	$V_{tot}, \mu\text{m}^3 \text{cm}^{-3}$	SSA
<i>In-situ measurements</i>							
June 06 -July 06	31 \pm 19	442 \pm 288	345 \pm 235	236 \pm 168	2.02 \pm 1.51	63 \pm 37	0.88 \pm 0.06
June 07–12 (EP1)	25 \pm 18	232 \pm 166	175 \pm 127	118 \pm 85	2.53 \pm 1.45	41 \pm 24	0.83 \pm 0.06
June 14–16 (EP2)	55 \pm 21	860 \pm 343	636 \pm 255	410 \pm 164	2.59 \pm 1.12	115 \pm 41	0.89 \pm 0.03
July 02–04 (EP3)	32 \pm 10	624 \pm 130	523 \pm 111	379 \pm 83	1.14 \pm 0.22	84 \pm 18	0.93 \pm 0.02
<i>Offline analysis</i>							
		OC, $\mu\text{g m}^{-3}$	EC, $\mu\text{g m}^{-3}$		Levoglucosan, ng m^{-3}		K^+ , $\mu\text{g m}^{-3}$
June 06 -July 06		17.8 \pm 8.9	3.6 \pm 1.7		264 \pm 433		1.5 \pm 1.4
June 07–12 (EP1)		14.6 \pm 5.5	3.5 \pm 1.8		158 \pm 151		0.8 \pm 0.4
June 14–16 (EP2)		43.8 \pm 4.4	6.1 \pm 1.6		1822 \pm 259		6.3 \pm 0.8
July 02–04 (EP3)		14.5 \pm 0.7	3.2 \pm 0.2		103 \pm 38		1.1 \pm 0.4

Table 2

Summary of number fractions of particles with different volatility and hygroscopicity. Avg. in the table means the campaign average; EP1, EP2 and EP3 denote the averages in the three episodes marked in Fig. 1.

Number fraction	50 nm				100 nm			
	Avg.	EP1	EP2	EP3	Avg.	EP1	EP2	EP3
NV	0.041 ± 0.066	0.034 ± 0.068	0.010 ± 0.020	0.075 ± 0.076	0.076 ± 0.054	0.085 ± 0.061	0.035 ± 0.029	0.101 ± 0.048
SV	0.409 ± 0.231	0.295 ± 0.207	0.755 ± 0.238	0.487 ± 0.117	0.431 ± 0.176	0.400 ± 0.168	0.752 ± 0.187	0.372 ± 0.100
HV	0.551 ± 0.247	0.670 ± 0.225	0.235 ± 0.231	0.438 ± 0.144	0.493 ± 0.179	0.514 ± 0.179	0.213 ± 0.173	0.526 ± 0.127
NH	0.120 ± 0.119	0.143 ± 0.153	0.190 ± 0.121	0.160 ± 0.081	0.095 ± 0.092	0.117 ± 0.115	0.095 ± 0.069	0.125 ± 0.084
SH	0.180 ± 0.143	0.246 ± 0.162	0.221 ± 0.141	0.163 ± 0.089	0.109 ± 0.117	0.158 ± 0.132	0.139 ± 0.065	0.059 ± 0.034
MH	0.700 ± 0.224	0.611 ± 0.264	0.589 ± 0.197	0.677 ± 0.149	0.796 ± 0.173	0.725 ± 0.201	0.766 ± 0.098	0.816 ± 0.104
Number fraction	150 nm				250 nm			
	Avg.	EP1	EP2	EP3	Avg.	EP1	EP2	EP3
NV	0.109 ± 0.062	0.130 ± 0.073	0.061 ± 0.028	0.120 ± 0.043	0.129 ± 0.088	0.187 ± 0.101	0.100 ± 0.140	0.104 ± 0.040
SV	0.424 ± 0.170	0.415 ± 0.168	0.722 ± 0.144	0.297 ± 0.056	0.384 ± 0.176	0.399 ± 0.167	0.644 ± 0.148	0.222 ± 0.040
HV	0.468 ± 0.176	0.455 ± 0.183	0.218 ± 0.134	0.584 ± 0.084	0.487 ± 0.202	0.415 ± 0.195	0.256 ± 0.117	0.675 ± 0.031
NH	0.107 ± 0.109	0.139 ± 0.134	0.086 ± 0.059	0.112 ± 0.078	0.115 ± 0.128	0.184 ± 0.159	0.112 ± 0.066	0.084 ± 0.073
SH	0.092 ± 0.096	0.103 ± 0.080	0.104 ± 0.057	0.043 ± 0.031	0.065 ± 0.113	0.060 ± 0.050	0.096 ± 0.037	0.012 ± 0.020
MH	0.801 ± 0.174	0.758 ± 0.179	0.810 ± 0.089	0.846 ± 0.099	0.820 ± 0.204	0.756 ± 0.189	0.792 ± 0.076	0.904 ± 0.083

showed a strong size-dependence, the VFRs of particles with different sizes in EP3 were very similar (Fig. 5C). In EP3, aerosol particles underwent intensive aging processes in highly polluted atmosphere and the secondary aerosol production somehow unified particle volatility and hygroscopicity properties. Wehner et al. (2009) showed that secondarily produced materials dominate the volume and mass of aerosol particles in polluted environment in Beijing.

As can be seen from Fig. 4E–H, the κ -PDFs in EP3 are dominated by MH mode particles with average number fractions ranging from 68% to 90%. The hygroscopicity of smaller particles (diameter 50, 100 nm) was similar in all episodes with an average MH $\kappa = 0.27$ and a number fraction of 67%. The biggest difference in hygroscopicity in the three episodes was observed between accumulation mode particles (150, 250 nm). In EP3, the number fraction of MH mode particles was approximately 13% higher than in EP1. The hygroscopicity of 250 nm MH mode particles in EP3 was close to pure ammonium sulfate (κ about 0.5–0.6) and further supporting the evidence that in highly polluted sulfur-rich environments, aerosol particle volatility and hygroscopicity are significantly influenced by heterogeneous reactions and condensation of sulfate onto preexisting particle surfaces (Pósfai et al., 2004).

Therefore, in our observed non-BB related pollution episode secondary aerosol formation was very likely to be driven by sulfate, while in the clean episode aerosol particles probably aged through the secondary organic aerosol production. These findings are consistent with previous works (Takegawa et al., 2009; Yue et al., 2009; Wehner et al., 2009; Liu et al., 2011).

3.3.2. Particle mixing state during the BB episode

Because the particle number concentration during the BB episode (EP2) is much higher than regular ambient level, we assumed that the observed particle physical-chemical properties during BB episode are dominated by BB aerosol. During the BB episode, the number fractions of NV and NH mode particles, which are related to fresh emissions, were much lower compared with other periods. In contrast to EP3, HV mode in EP2 tailed away with increasing particle diameter. The dominant volatile mode centered at SF = 0.6 with a number fraction of 80%, which is 43% higher than the campaign average. All these results suggested that in terms of mixing state, aerosol particles originating from BB were significantly different from those from other episodes. Aerosol particles from BB did not carry thick hygroscopic and volatile coatings as particles from the non-BB pollution episode. In fact, BB originated

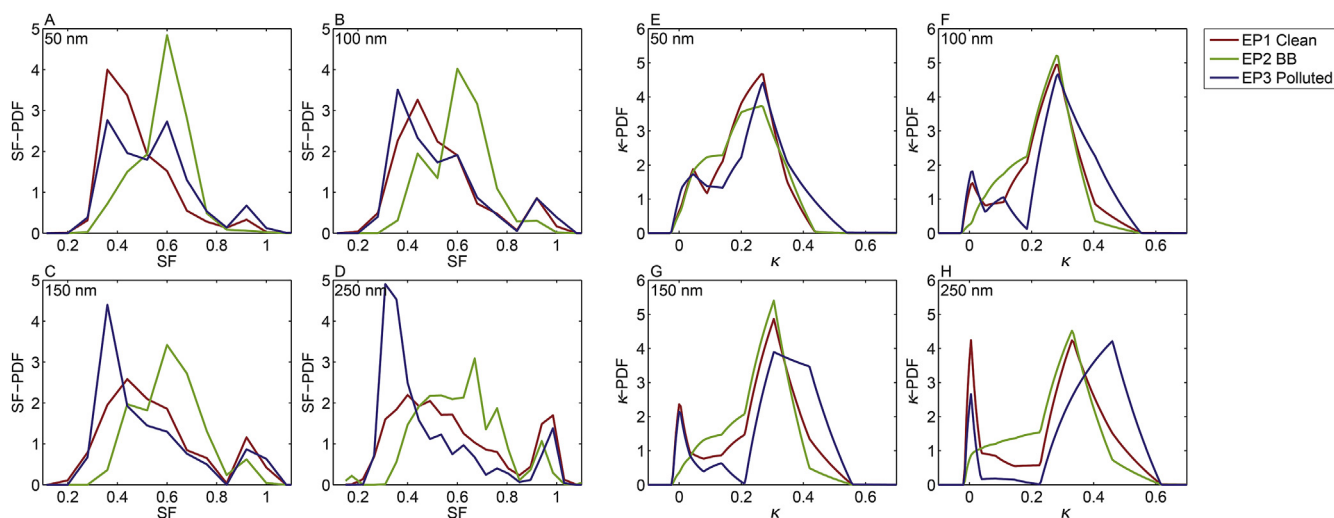


Fig. 4. Average probability density functions of shrink factor (A–D) and hygroscopicity parameter κ (E–H) at measured particles sizes for the three selected episodes.

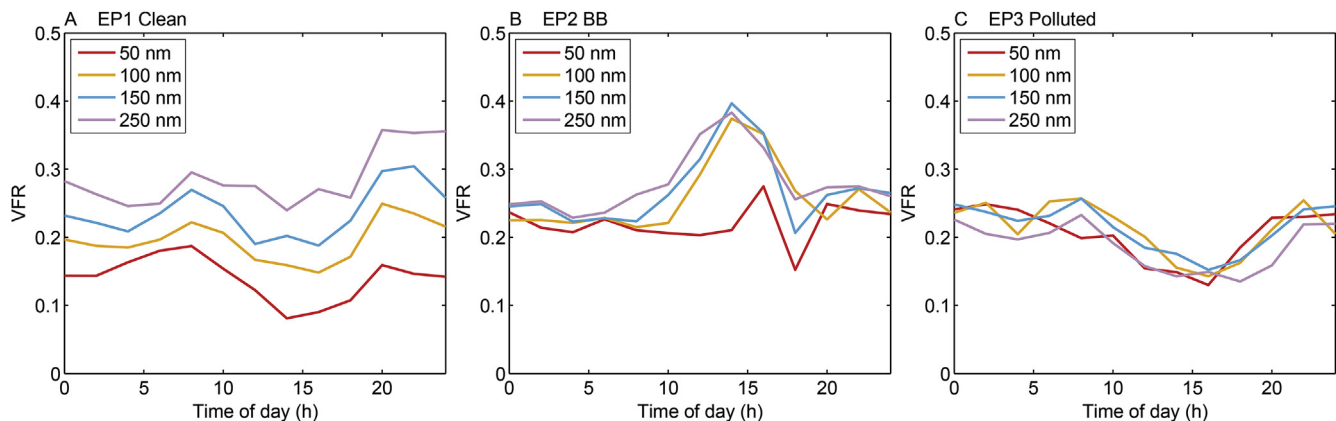


Fig. 5. Diurnal variation of particle volume fraction remaining (VFR) at 300 °C during clean (A), BB (B) and pollution (C) episode.

particles were less volatile than in other episodes. This can be seen in the VFR of particles larger than 100 nm, which ranges from 25% to 40% in BB episode; while during clean and non-BB related pollution episodes particle VFR were in a range from 20% to 30% (Fig. 5). Interestingly, 50 nm particles did not follow the trend of bigger particles in EP2. This suggests that particles produced in BB are mainly in accumulation mode. The dip in VFR in EP2 at 18:00 LT is the result of missing values.

In terms of hygroscopicity, the MH mode in the BB episode centered between κ of 0.25 and 0.33. Larger particles showed higher values of κ , which was comparable to the values observed in EP1. The MH mode in the BB episode was slightly narrower and its number fraction was only marginally higher than in other episodes. Narrower distribution of MH mode with higher peak value resulted in MH mode number fraction similar to EP1 ~ 77%. The same was also true for SH and NH mode particle number fractions. Therefore, we may conclude that our observed BB originated aerosol particles did not have higher hygroscopicity, at least not higher than in the other predefined periods.

To answer the question, which kind of aerosol particles and which processes resulted in a mixing state of BB aerosol, we have to clarify the constituents of BB emission and then discuss their volatility properties. The non-volatile (at 300 °C) species originating from BB may include: potassium salts that decompose between 400 °C and 1700 °C (Knudsen et al., 2004), EC that decompose at around 900 °C (Jennings et al., 1994), and organic matter of which the majority was found to be semi- or non-volatile (Poulain et al., 2014). As mentioned above, Pósfai et al. (2004) also found tar ball (TB) is rich in BB aerosol. All mentioned BB products may form an externally mixed NV or/and SV mode in a volatility distribution after being treated thermally. This external mixture of BB particles was already found at the emission source in previous studies (e.g. Li et al., 2003). However, in our study, we did not observe any increase in the NV mode particle number fraction during the BB episode. We explain this as follows. During the BB episode, high numbers non-volatile particles were emitted from BB. Since the number concentration of particles created in the combustion process was significantly higher than the background particle concentration, BB originated particles became the dominant in the environment. Before being observed, those particles aged in the air mass during the long range transport. On one hand, coated with secondary produced species with higher volatility, BB products may have turned to be more volatile. On the other hand, the transformation of volatile organic compounds to low-volatility organic matter may have changed BB particles to be less volatile. Such atmospheric processing of BB particles was already observed

both in laboratory and field studies. For example, Capes et al. (2008) investigated aerosol in BB plume over West Africa based on aircraft measurements with an aerosol mass spectrometer onboard. The abundance of low-volatility organic matter was explained by atmospheric aging. In laboratory studies, Hennigan et al. (2011) found that photo-oxidation chemically and physically transformed (via condensation and aerosol processing) the organic aerosol including decrease in particle volatility with aging. Tritscher et al. (2011) also showed that particle volatility can be reduced due to OH and O₃ induced condensation. Secondary organic aerosol mass production through functionalization or fragmentation increased particle oxidative state, which made particles even less volatile. The competition of above mentioned atmospheric processes may have determined our observed broadened SF-PDFs of BB originated particles.

3.3.3. Implication on SSA

Previously, we have shown that aerosol particles, produced in biomass burning, are explicitly different in terms of mixing state compared to particles in other episodes (Fig. 4). Thus, it is important to evaluate what effect BB originated aerosol has on the aerosol optical particle properties which determines the aerosol direct radiative forcing. SSA, defined as the ratio of light scattering coefficient to total light extinction coefficient (a sum of scattering and absorption), is a dominant parameter in the estimation of aerosol radiative effects and is also important in satellite retrieval algorithms (McComiskey et al., 2008). Mishchenko et al. (2004) reported that an accuracy of 0.03 and a precision of 0.02 in the determination of the SSA are required for a reliable quantification of aerosol direct and semi-direct effects on climate. Even small biases in SSA may result in large uncertainties (Takemura et al., 2002).

To evaluate the impact of BB on the SSA of ambient aerosol, SSA at different RHs was simulated using the measured aerosol physical-chemical properties. The calculation is based on the methodology presented by Ma et al. (2014) and will not be discussed in detail here. Shortly, three conceptual models of BC mixing state - external mixture (EXT), homogeneous internal mixture (INT), and core-shell internal mixture (CS), were employed to simulate SSA using the BHMIE and BHCOAT models (Bohren and Huffman, 1983; Ma et al., 2014). These three conceptual models have been widely used to assess aerosol optical properties and direct radiative forcing (Jacobson, 2001; Ma et al., 2012). To implement the simulations of the state of mixing to derive the SSA, several assumptions had to be made. Firstly, BC volume fraction was assumed to be constant in sub-micron size range, and 0 in super-

micron size range. PNSD at a certain RH was calculated based on the measured size-resolved κ (averaged from κ -PDF). The refractive indices of BC and other particle species are assumed to be $1.75-0.55i$ and $1.53-10^{-6}i$, respectively. And the density of BC was assumed to be 1.5 g cm^{-3} . The calculation of SSA at RH from 50% to 95% was respectively done for the three selected episodes, based on the average PNSD, BC mass concentration and aerosol hygroscopicity for each episode.

Considering that assuming constant refractive indices of aerosol species and density of BC is arbitrary, Monte Carlo approach was used to estimate the uncertainty of the calculated SSA induced by this assumption. The uncertainty (assumed to be 3σ hereinafter) of the density of BC was set to 33% to cover the values reported in literature, $1.00-2.00 \text{ g cm}^{-3}$ (Sloane, 1983, 1984, 1991; Sloane and Wolff, 1985; Ouimette and Flagan, 1982; Seinfeld et al., 1998). The uncertainties of the refractive indices were also set in the similar way according to literature (Ouimette and Flagan, 1982; Hasan and Dzubay, 1983; Sloane, 1984; Seinfeld et al., 1998; Covert et al., 1990; Tang and Munkelwitz, 1994). For refractive index of BC, it was assumed to be 12% and 20% for real part and imaginary part, respectively. And for the refractive index of other species it was assumed to be 33% and 1.5%, respectively. The detail of the Monte Carlo simulation can be found in Ma et al. (2014).

Fig. 6 displays the results of the simulation. The shaded areas show the standard deviations of the calculated SSA obtained from the Monte Carlo approach. It can be seen that with the same aerosol mixing state, the differences between the SSA for the three episodes are significant. At RH of 50%, the difference between SSA in pollution episode and clean episode can be up to 0.8. Although the differences decrease with increasing RH, they are still higher than the standard deviation of SSA. It means that the variation of SSA in different pollution conditions needs to be considered in the evaluation of aerosol direct radiative effects in the NCP.

It also can be seen in Fig. 6 that SSA is quite sensitive on the mixing state of BC, especially at low-RH condition. The differences between SSA for mixing state of INT and EXT range from about 0.6 to 0.9 for the three episodes, at RH of 50%. This difference decreases with the increase of RH, and is around 0.3 at RH of 95%. However, the SSA calculated based on mixing state of INT and CS are very similar at whole RH range in Fig. 6.

The average measured SSA at dry state during the three episodes are also shown in the left side of Fig. 6. The error bar shows the temporal variability of the measurements. It can be found that for all the three episodes, the measured SSA are very close to the calculated ones with assumed mixing states of INT and CS, but much lower than the SSA with assumed mixing state of EXT. The conceptual model of CS mixing is usually suggested for calculation of aerosol radiative properties (Jacobson, 2001; Chandra et al., 2004; Katrinak et al., 1992, 1993; Ma et al., 2012). Our calculation indicates that both CS and INT model are appropriate for the calculation of ambient SSA in the NCP. And the SSA will be significantly over-predicted if EXT mixing is assumed.

4. Summary and conclusions

Atmospheric aerosol particle physical and chemical properties were measured at a regional site in the North China Plain in the frame of the CAREBeijing-NCP project in summer 2014. The primary focus of this case study was to determine the mixing state of particles originating from biomass burning and to find how the particle mixing state influences aerosol optical properties.

During the biomass burning episode defined with high concentration of anhydrosugar levoglucosan and water soluble potassium, the probability density function of shrink factor showed a different shape compared with other selected episodes. The reduction in highly volatile and non-volatile particle number fractions together with a simultaneous increase in semi-volatile particle number fraction have shaped the shrink factor probability density function so that the maximum of was found at shrink factor of 0.6 with a number fraction of semi-volatile particles reaching 70%. The non-volatile particle number fraction during the biomass burning episode decreased to 3% and was the lowest measured value compared to all other predefined episodes. Particle volume fraction remaining increased to approximately 25–40%, while in the clean and non-biomass burning related episodes the volume fraction remaining varied around 20%. In terms of hygroscopicity, particles originating from biomass burning showed a similar PDF of hygroscopicity parameter κ as that observed in the clean episode, but largely differed from the non-biomass burning related pollution episode during which accumulation mode

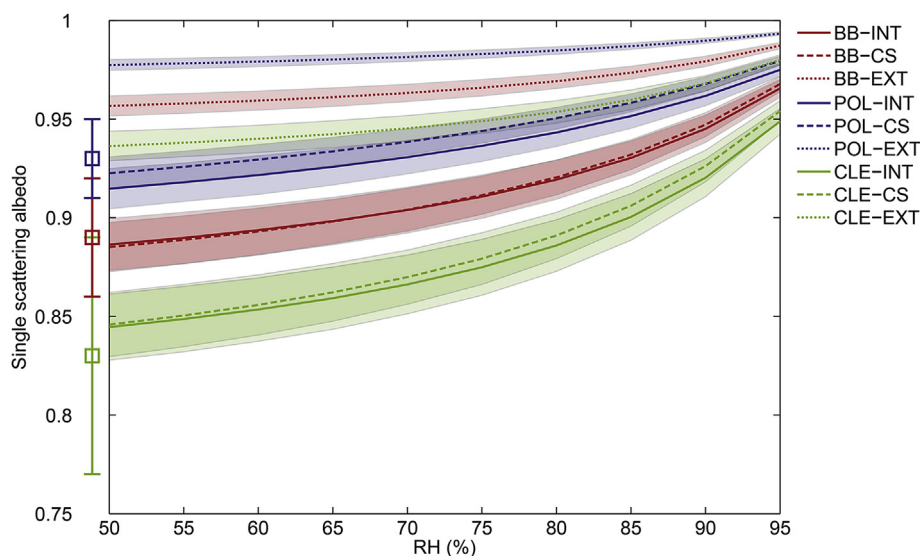


Fig. 6. Simulated SSA at different relative humidities (RHs) for biomass burning episode (BB), pollution episode (POL) and clean episode (CLE). Here INT, CS and EXT denotes homogeneously internal, core-shell internal, and external mixing state models, respectively. The shaded areas show the standard deviations of the calculated SSA obtained from the Monte Carlo simulation. The average measured SSA at dry condition is marked as squares in the left side, with the errorbars denotes the standard deviation of the time series.

particles showed a higher hygroscopicity.

To evaluate the influence of particle mixing state on aerosol single scattering albedo, SSA at different RHs was simulated using the measured aerosol physical-chemical properties. And Monte Carlo approach was used to estimate the uncertainty of the calculation. It was found that the differences between the calculated SSA for biomass burning, clean and pollution episodes are significant, meaning that the variation of SSA in different pollution conditions needs to be considered in the evaluation of aerosol direct radiative effects in the NCP. We also found that SSA is quite sensitive on the mixing state of BC, especially at low-RH condition. The differences between SSA for internal and external mixing range from about 0.6 to 0.9 at RH of 50%. The simulated SSA was also compared with the measured values. For all the three predefined episodes, the measured SSA are very close to the calculated ones with assumed mixing states of homogeneously internal and core-shell internal mixing, indicating that both homogeneously internal and core-shell internal models are appropriate for the calculation of ambient SSA in the NCP.

Acknowledgment

This research is supported by the projects Sino German Science center (No. GZ663) and National Basic Research Program of China (Nos. 2013CB955801, 2013CB228503), and the National Natural Science Foundation of China (Nos. 21190052, 41305030, 41121004, 41175030). Travelling costs for CAREBeijing-NCP 2014 were partly funded by the EU project AMIS 295132.

References

- Anderson, T.L., Covert, D.S., Marshall, S.F., Laucks, M.L., Charlson, R.J., Waggoner, A.P., Ogren, J.A., Caldow, R., Holm, R.L., Quant, G., Sem, J., Wiedensohler, A., Ahlquist, N.A., Bates, T.S., 1996. Performance characteristics of a High-sensitivity, three-wavelength total scatter/backscatter nephelometer. *J. Atmos. Ocean. Technol.* 13, 967–986.
- Andreae, M.O., Merlet, P., 2001. Emission of trace gases and aerosols from biomass burning. *Glob. Biogeochem. Cycles* 15, 955–966.
- Bi, X.H., Zhang, G.H., Li, L., Wang, X.M., Li, M., Sheng, G.Y., Fu, J.M., Zhou, Z., 2011. Mixing state of biomass burning particles by single particle aerosol mass spectrometer in the urban area of PRD, China. *Atmos. Environ.* 45, 3447–3453. <http://dx.doi.org/10.1016/j.atmosenv.2011.03.034>.
- Birmili, W., Heinke, K., Pitz, M., Matschullat, J., Wiedensohler, A., Cyrys, J., Wichmann, H.-E., Peters, A., 2010. Particle number size distributions in urban air before and after volatilisation. *Atmos. Chem. Phys.* 10, 4643–4660. <http://dx.doi.org/10.5194/acp-10-4643-2010>.
- Bohren, C.F., Huffman, D.R., 1983. *Absorption and Scattering of Light by Small Particles*. John Wiley, Hoboken, N. J.
- Capes, G., Johnson, B., McFiggans, G., Williams, P.I., Haywood, J., Coe, H., 2008. Aging of biomass burning aerosols over West Africa: aircraft measurements of chemical composition, microphysical properties, and emission ratios. *J. Geophys. Res.* 113 <http://dx.doi.org/10.1029/2008JD009845>.
- Cavalli, F., Viana, M., Yttri, K.E., Genberg, J., Pataud, J.P., 2010. Toward a standardised thermal-optical protocol for measuring atmospheric organic and elemental carbon: the EUSAAR protocol. *Atm. Meas. Tech.* 3 (1), 79–89.
- Chandra, S., Satheesh, S.K., Srinivasan, J., 2004. Can the state of mixing of black carbon aerosols explain the mystery of 'excess' atmospheric absorption? *Geophys. Res. Lett.* 31 (19).
- Cheng, Y., Engling, G., He, K.B., Duan, F.K., Ma, Y.L., Du, Z.Y., Liu, J.M., Zheng, M., Weber, R.J., 2013. Biomass burning contribution to Beijing aerosol. *Atmos. Chem. Phys.* 13, 7765–7781. <http://dx.doi.org/10.5194/acp-13-7765-2013>.
- Christopher, S.A., Kliche, D.V., Chou, J., et al., 1996. First estimates of the radiative forcing of aerosols generated from biomass burning using satellite data[J]. *J. Geophys. Res. Atmos.* 101 (D16), 21265–21273.
- Chung, C.E., Lee, K., Muller, D., 2012. Effect of internal mixture on black carbon radiative forcing. *Tellus* 64B, 10925. <http://dx.doi.org/10.3042/tellusb.v64i0.10925>.
- Covert, D.S., Heintzenberg, J., Hansson, H.C., 1990. Electro-optical detection of external mixtures in aerosols. *Aerosol Sci. Technol.* 12 (2), 446–456.
- Draxler, R.R., Rolph, G.D., 2013. HYSPLIT (Hybrid Single-particle Lagrangian Integrated Trajectory) Model Access via NOAA ARL READY Website. NOAA Air Resources Laboratory, Silver Spring, Md. <http://ready.arl.noaa.gov/HYSPLIT.php>.
- Ehn, M., Thornton, J.A., Kleist, E., Sipilä, M., Junninen, H., Pullinen, I., Springer, M., Rubach, F., Tillmann, R., Lee, B., 2014. Large source of low-volatility secondary organic aerosol. *Nature* 506, 476–479.
- Godfray, H.C.J., Beddington, J.R., Crute, I.R., Haddad, L., Lawrence, D., Muir, J.F., Pretty, J., Robinson, S., Thomas, S.M., Toulmin, C., 2010. Food security: the challenge of feeding 9 billion people. *Science* 327 (5967), 812–818.
- Gysel, M., McFiggans, G.B., Coe, H., 2009. Inversion of tandem differential mobility analyser (TDMA) measurements. *J. Aerosol Sci.* 40, 134–151. <http://dx.doi.org/10.1016/j.jaerosci.2008.07.013>.
- Hasan, H., Dzubay, T.G., 1983. Apportioning light extinction coefficients to chemical species in atmospheric aerosol. *Atmos. Environ.* 17 (8), 1573–1581, 1967.
- Heintzenberg, J., Charlson, R.J., 1996. Design and applications of the integrating nephelometer: a review. *J. Atmos. Ocean. Technol.* 13 (5), 987–1000.
- Hennig, T., Massling, A., Brechtel, F.J., Wiedensohler, A., 2005. A tandem DMA for highly temperature-stabilized hygroscopic particle growth measurements between 90% and 98% relative humidity. *J. Aerosol Sci.* 36, 1210–1223. <http://dx.doi.org/10.1016/j.jaerosci.2005.01.005>.
- Hennigan, C.J., Miracolo, M.A., Engelhart, G.J., May, A.A., Presto, A.A., Lee, T., Sullivan, A.P., McMeeking, G.R., Coe, H., Wold, C.E., Hao, W.-M., Gilman, J.B., Kuster, W.C., de Gouw, J., Schichtel, B.A., Collett Jr., J.L., Kreidenweis, S.M., Robinson, A.L., 2011. Chemical and physical transformations of organic aerosol from the photo-oxidation of open biomass burning emissions in an environmental chamber. *Atmos. Chem. Phys.* 11, 7669–7686. <http://dx.doi.org/10.5194/acp-11-7669-2011>.
- Hobbs, P.V., Reid, J.S., Kotchenruther, R.A., et al., 1997. Direct radiative forcing by smoke from biomass burning. *Science* 275 (5307), 1777–1778.
- Hyvärinen, A.-P., Vakkari, V., Laakso, L., Hooda, R.K., Sharma, V.P., Panwar, T.S., Beukes, J.P., van Zyl, P.G., Josipovic, M., Garland, R.M., Andreae, M.O., Pöschl, U., Petzold, A., 2013. Correction for a measurement artifact of the Multi-Angle Absorption Photometer (MAAP) at high black carbon mass concentration levels. *Atmos. Meas. Tech.* 6, 81–90. <http://dx.doi.org/10.5194/amt-6-81-2013>.
- Iinuma, Y., Engling, G., Puxbaum, H., Herrmann, H., 2009. A highly resolved anion-exchange chromatographic method for determination of saccharidic tracers for biomass combustion and primary bio-particles in atmospheric aerosol. *Atmos. Environ.* 43, 1367–1371.
- Jacob, D.J., Crawford, J.H., Kleb, M.M., Connors, V.S., Bendura, R.J., Raper, J.L., Sachse, G.W., Gille, J.C., Emmons, L., Heald, C.L., 2003. Transport and Chemical Evolution over the Pacific (TRACE-P) aircraft mission: design, execution, and first results. *J. Geophys. Res.* 108 (D20) <http://dx.doi.org/10.1029/2002JD003276>.
- Jacobson, M.Z., 2001. Strong radiative heating due to the mixing state of black carbon in atmospheric aerosols. *Nature* 409, 695–697.
- Jaffe, D., McKendry, I., Anderson, T., Price, H., 2003. Six new episodes of trans-Pacific transport of air pollutants. *Atmos. Environ.* 37 (3), 391–404.
- Jennings, S.G., O'Dowd, C.D., Cooke, W.F., Sheridan, P.J., Cachier, H., 1994. Volatility of elemental carbon. *Geophys. Res. Lett.* 21, 1719–1722.
- Jeong, S.J., Ho, C.H., Piao, S., Kim, J., Ciais, P., Lee, Y.B., Jhun, J.G., Park, S.K., 2014. Effects of double-cropping on summer climate of the North China Plain and neighbouring regions. *Nat. Clim. Change* 4 (7), 615–619.
- Katrinak, K.A., Rez, P., Buseck, P.R., 1992. Structural variations in individual carbonaceous particles from an urban aerosol. In: *Environmental Science & Technology*.
- Katrinak, K.A., Rez, P., Perkes, P.R., Buseck, P.R., 1993. Fractal geometry of carbonaceous aggregates from an urban aerosol. *Environ. Sci. Technol.* 27 (3), 539–547.
- Kecorius, S., Zhang, S., Wang, Z., Gröss, J., Ma, N., Wu, Z., Ran, L., Hu, M., Wang, P., Ulevicvics, V., Wiedensohler, A., 2015. Nocturnal aerosol particle formation in the North China Plain. *Lith. J. Phys.* 55, 44–53.
- Knudsen, J.N., Jensen, P.A., Johansen, D.K., 2004. Transformation and release to the gas phase of Cl, K, and S during combustion of annual biomass. *Energy Fuels* 18 (5), 1385–1399.
- Lan, Z.J., Huang, X.F., Yu, K.Y., Sun, T.L., Zeng, L.W., Hu, M., 2013. Light absorption of black carbon aerosol and its enhancement by mixing state in an urban atmosphere in South China. *Atmos. Environ.* 69, 118–123.
- Li, J., Pósfai, M., Hobbs, P.V., Buseck, P.R., 2003. Individual aerosol particles from biomass burning in southern Africa: 2. Compositions and aging of inorganic particles. *J. Geophys. Res.* 108 (D13), 4844. <http://dx.doi.org/10.1029/2002JD002310>.
- Liu, P.F., Zhao, C.S., Göbel, T., Hallbauer, E., Nowak, A., Ran, L., Xu, W.Y., Deng, Z.Z., Ma, N., Mildnerberger, K., Henning, S., Stratmann, F., Wiedensohler, A., 2011. Hygroscopic properties of aerosol particles at high relative humidity and their diurnal variations in the North China Plain. *Atmos. Chem. Phys.* 11, 3479–3494. <http://dx.doi.org/10.5194/acp-11-3479-2011>.
- Ma, N., Zhao, C.S., Nowak, A., Müller, T., Pfeifer, S., Cheng, Y.F., Deng, Z.Z., Liu, P.F., Xu, W.Y., Ran, L., Yan, P., Göbel, T., Hallbauer, E., Mildnerberger, K., Henning, S., Yu, J., Chen, L.L., Zhou, X.J., Stratmann, F., Wiedensohler, A., 2011. Aerosol optical properties in the North China Plain during HaChi campaign: an in-situ optical closure study. *Atmos. Chem. Phys.* 11, 5959–5973. <http://dx.doi.org/10.5194/acp-11-5959-2011>.
- Ma, N., Zhao, C.S., Müller, T., Cheng, Y.F., Liu, P.F., Deng, Z.Z., Xu, W.Y., Ran, L., Nekat, B., van Pinxteren, D., Gnauk, T., Müller, K., Herrmann, H., Yan, P., Zhou, X.J., Wiedensohler, A., 2012. A new method to determine the mixing state of light absorbing carbonaceous using the measured aerosol optical properties and number size distributions. *Atmos. Chem. Phys.* 12, 2381–2397. <http://dx.doi.org/10.5194/acp-12-2381-2012>.
- Ma, N., Birmili, W., Müller, T., Tuch, T., Cheng, Y.F., Xu, W.Y., Zhao, C.S., Wiedensohler, A., 2014. Tropospheric aerosol scattering and absorption over central Europe: a closure study for the dry particle state. *Atmos. Chem. Phys.* 14, 6241–6259. <http://dx.doi.org/10.5194/acp-14-6241-2014>.
- McComiskey, A., Schwartz, S.E., Schmid, B., Guan, H., Lewis, E.R., Ricchiuzzi, P.,

- Ogren, J.A., 2008. Direct aerosol forcing: calculation from observables and sensitivities to inputs. *J. Geophys. Res. Atmos.* 113, D09202. <http://dx.doi.org/10.1029/2007JD009170>.
- Mishchenko, M.I., Cairns, B., Hansen, J.E., Travis, L.D., Burg, R., Kaufman, Y.J., Martins, J.V., Shettle, E.P., 2004. Monitoring of aerosol forcing of climate from space: analysis of measurement requirements. *J. Quant. Spectro. Rad. Trans.* 88, 149–161. <http://dx.doi.org/10.1016/j.jqsrt.2004.03.030>.
- Nastos, P.T., Paliatatos, A.G., Anthracopoulos, M.B., Roma, E.S., Priftis, K.N., 2010. Outdoor particulate matter and childhood asthma admissions in Athens, Greece: a time-series study. *Environ. Health* 9, 45.
- Ni, H., Han, Y., Cao, J., Chen, L.W.A., Tian, J., Wang, X., Chow, J.C., Watson, J.G., Wang, Q., Wang, P., Li, H., 2015. Emission characteristics of carbonaceous particles and trace gases from open burning of crop residues in China. *Atmos. Environ.* 123, 399–406.
- Nordmann, S., Cheng, Y.F., Carmichael, G.R., Yu, M., Denier van der Gon, H.A.C., Zhang, Q., Saide, P.E., Pöschl, U., Su, H., Birmili, W., Wiedensohler, A., 2014. Atmospheric black carbon and warming effects influenced by the source and absorption enhancement in central Europe. *Atmos. Chem. Phys.* 14, 12683–12699. <http://dx.doi.org/10.5194/acp-14-12683-2014>.
- Ouimette, J.R., Flagan, R.C., 1982. The extinction coefficient of multicomponent aerosols. *Atmos. Environ.* 16 (10), 2405–2419, 1967.
- Peters, M.D., Kreidenweis, S.M., 2007. A single parameter representation of hygroscopic growth and cloud condensation nucleus activity. *Atmos. Chem. Phys.* 7, 1961–1971. <http://dx.doi.org/10.5194/acp-7-1961-2007>.
- Petzold, A., Schönlinner, M., 2004. The Multi-angle absorption photometer – a new method for the measurement of aerosol light absorption and atmospheric black carbon. *J. Aerosol Sci.* 35, 421–441.
- Pfeifer, S., Birmili, W., Schladitz, A., Müller, T., Nowak, A., Wiedensohler, A., 2014. A fast and easy-to-implement inversion algorithm for mobility particle size spectrometers considering particle number size distribution information outside of the detection range. *Atmos. Meas. Tech.* 7, 95–105. <http://dx.doi.org/10.5194/amt-7-95-2014>.
- Philippin, S., Wiedensohler, A., Stratmann, F., 2004. Measurements of non-volatile fractions of pollution aerosols with an eight-tube volatility tandem differential mobility analyzer (VTDMA-8). *J. Aerosol Sci.* 35, 185–203.
- Pirrone, N., Cinnirella, S., Feng, X., Finkelman, R.B., Friedli, H.R., Leaner, J., Mason, R., Mukherjee, A.B., Stracher, G.B., Streets, D.G., Telmer, K., 2010. Global mercury emissions to the atmosphere from anthropogenic and natural sources. *Atmos. Chem. Phys.* 10 (13), 5951–5964.
- Pósfai, M., Gelencsér, A., Simonics, R., Arató, K., Li, J., Hobbs, P.V., Buseck, P.R., 2004. Atmospheric tar balls: particles from biomass and biofuel burning. *J. Geophys. Res. Atmos.* 109 (D6) <http://dx.doi.org/10.1029/2003JD004169>.
- Poulain, L., Birmili, W., Canonaco, F., Crippa, M., Wu, Z.J., Nordmann, S., Spindler, G., Prévôt, A.S.H., Wiedensohler, A., Herrmann, H., 2014. Chemical mass balance of 300 °C non-volatile particles at the tropospheric research site Melpitz. *Ger. Atmos. Chem. Phys.* 14, 10145–10162. <http://dx.doi.org/10.5194/acp-14-10145-2014>.
- Pratt, K.A., Murphy, S.M., Subramanian, R., DeMott, P.J., Kok, G.L., Campos, T., Rogers, D.C., Prenni, A.J., Heymsfield, A.J., Seinfeld, J.H., Prather, K.A., 2011. Flight-based chemical characterization of biomass burning aerosols within two prescribed burn smoke plumes. *Atmos. Chem. Phys.* 11, 12549–12565. <http://dx.doi.org/10.5194/acp-11-12549-2011>.
- Rader, D.J., McMurry, P.H., 1986. Application of the tandem differential mobility analyzer to studies of droplet growth or evaporation. *J. Aerosol Sci.* 17 (5), 771–787.
- Reid, J.S., Koppmann, R., Eck, T.F., Eleuterio, D.P., 2005. A review of biomass burning emissions part II: intensive physical properties of biomass burning particles. *Atmos. Chem. Phys.* 5, 799–825. <http://dx.doi.org/10.5194/acp-5-799-2005>.
- Rolph, G.D., 2013. Real-time Environmental Applications and Display System (READY). NOAA Air Resources Laboratory, College Park, MD. <http://www.ready.noaa.gov>.
- Seinfeld, J.H., Pandis, S.N., Noone, K., 1998. *Atmospheric Chemistry and Physics: from Air Pollution to Climate Change*.
- Simoneit, B.R.T., Schauer, J.J., Nolte, C.G., Oros, D.R., Elias, V.O., Fraser, M.P., Rogge, W.F., Cass, G.R., 1999. Levoglucosan, a tracer for cellulose in biomass burning and atmospheric particles. *Atmos. Environ.* 33, 173–182. [http://dx.doi.org/10.1016/S1352-2310\(98\)00145-9](http://dx.doi.org/10.1016/S1352-2310(98)00145-9).
- Sloane, C.S., 1983. Optical properties of aerosols—comparison of measurements with model calculations. *Atmos. Environ.* 17 (2), 409–416, 1967.
- Sloane, C.S., 1984. Optical properties of aerosols of mixed composition. *Atmos. Environ.* 18 (4), 871–878, 1967.
- Sloane, C.S., Wolff, G.T., 1985. Prediction of ambient light scattering using a physical model responsive to relative humidity: validation with measurements from Detroit. *Atmos. Environ.* 19 (4), 669–680, 1967.
- Sloane, C.S., Watson, J., Chow, J., Pritchett, L., Richards, L.W., 1991. Size-segregated fine particle measurements by chemical species and their impact on visibility impairment in Denver. *Atmos. Environ. Part A. General Top.* 25 (5–6), 1013–1024.
- Takegawa, N., Miyakawa, T., Kuwata, M., Kondo, Y., Zhao, Y., Han, S., Kita, K., Miyazaki, Y., Deng, Z., Xiao, R., Hu, M., 2009. Variability of submicron aerosol observed at a rural site in Beijing in the summer of 2006. *J. Geophys. Res. Atmos.* 114, D00G05. <http://dx.doi.org/10.1029/2008JD010857>.
- Takekuma, T., Nakajima, T., Dubovik, O., Holben, B.N., Kinne, S., 2002. Single scattering albedo and radiative forcing of various aerosol species with a global three dimensional model. *J. Clim.* 15, 333–352.
- Tang, I.N., Munkelwitz, H.R., 1994. Water activities, densities, and refractive indices of aqueous sulfates and sodium nitrate droplets of atmospheric importance. *J. Geophys. Res.* 99 (D9), 18801–18808.
- Tivanski, A.V., Hopkins, R.J., Tylliszczak, T., Gilles, M.K., 2007. Oxygenated interface on biomass burn tar balls determined by single particle scanning transmission X-ray microscopy. *J. Phys. Chem. A* 111, 5448–5458.
- Tóth, A., Hoffer, A., Nyiró-Kósa, I., Pósfai, M., Gelencsér, A., 2014. Atmospheric tar balls: aged primary droplets from biomass burning? *Atmos. Chem. Phys.* 14, 6669–6675. <http://dx.doi.org/10.5194/acp-14-6669-2014>.
- Tritscher, T., Dommen, J., DeCarlo, P.F., Gysel, M., Barmet, P.B., Praplan, A.P., Weingartner, E., Prévôt, A.S.H., Riipinen, I., Donahue, N.M., Baltensperger, U., 2011. Volatility and hygroscopicity of aging secondary organic aerosol in a smog chamber. *Atmos. Chem. Phys.* 11 (22), 11477–11496.
- Tuch, T.M., Haudek, A., Müller, T., Nowak, A., Wex, H., Wiedensohler, A., 2009. Design and performance of an automatic regenerating adsorption aerosol dryer for continuous operation at monitoring sites. *Atmos. Meas. Tech.* 2, 417–422. <http://dx.doi.org/10.5194/amt-2-417-2009>.
- Wang, Q., Huang, R.J., Cao, J., Han, Y., Wang, G., Li, G., Wang, Y., Dai, W., Zhang, R., Zhou, Y., 2014. Mixing state of black carbon aerosol in a heavily polluted urban area of China: implications for light absorption enhancement. *Aerosol Sci. Technol.* 48, 689–697. <http://dx.doi.org/10.1080/02786826.2014.917758>.
- Wehner, B., Birmili, W., Ditas, F., Wu, Z., Hu, M., Liu, X., Mao, J., Sugimoto, N., Wiedensohler, A., 2008. Relationships between submicrometer particulate air pollution and air mass history in Beijing, China, 2004–2006. *Atmos. Chem. Phys.* 8 (20), 6155–6168.
- Wehner, B., Berghof, M., Cheng, Y.F., Achtert, P., Birmili, W., Nowak, A., Wiedensohler, A., Garland, R.M., Pöschl, U., Hu, M., Zhu, T., 2009. Mixing state of nonvolatile aerosol particle fractions and comparison with light absorption in the polluted Beijing region. *J. Geophys. Res. Atmos.* 114 (D2).
- Wiedensohler, A., Orsini, D., Covert, D.S., Coffmann, D., Cantrell, W., Havlicek, M., Brechtel, F.J., Russell, L.M., Weber, R.J., Gras, J., Hudson, J.G., Litchy, M., 1997. Intercomparison study of the size-dependent counting efficiency of 26 condensation particle counters. *Aerosol Sci. Technol.* 27, 224–242.
- Wiedensohler, A., Cheng, Y.F., Nowak, N., Wehner, B., Achtert, P., Berghof, M., Birmili, W., Wu, Z.J., Hu, M., Zhu, T., Takegawa, N., Kita, K., Kondo, Y., Lou, S.R., Hofzumahaus, A., Holland, F., Wahner, A., Gunthe, S.S., Rose, D., Pöschl, U., 2009. Rapid aerosol particle growth and increase of cloud condensation nucleus activity by secondary aerosol formation and condensation: a case study for regional air pollution in northeastern China. *JGR* 114. <http://dx.doi.org/10.1029/2008JD010884>.
- Wiedensohler, A., Birmili, W., Nowak, A., Sonntag, A., Weinhold, K., Merkel, M., Wehner, B., Tuch, T., Pfeifer, S., Fiebig, M., Fjåraa, A.M., Asmi, E., Sellegri, K., Depuy, R., Venzac, H., Villani, P., Laj, P., Aalto, P., Ogren, J.A., Swietlicki, E., Williams, P., Roldin, P., Quincey, P., Hüglin, C., Fierz-Schmidhauser, R., Gysel, M., Weingartner, E., Riccobono, F., Santos, S., Grünig, C., Faloon, K., Beddows, D., Harrison, R., Monahan, C., Jennings, S.G., O'Dowd, C.D., Marinoni, A., Horn, H.-G., Keck, L., Jiang, J., Scheckman, J., McMurry, P.H., Deng, Z., Zhao, C.S., Moerman, M., Henzing, B., de Leeuw, G., Löschau, G., Bastian, S., 2012. Mobility particle size spectrometers: harmonization of technical standards and data structure to facilitate high quality long-term observations of atmospheric particle number size distributions. *Atmos. Meas. Tech.* 5, 657–685. <http://dx.doi.org/10.5194/amt-5-657-2012>.
- Wu, Z.J., Hu, M., Liu, S., Wehner, B., Bauer, S., Maßling, A., Wiedensohler, A., Petäjä, T., Dal Maso, M., Kulmala, M., 2007. New particle formation in Beijing, China: statistical analysis of a 1-year data set. *J. Geophys. Res.* 112, D09209. <http://dx.doi.org/10.1029/2006JD007406>.
- Yue, D., Hu, M., Wu, Z., Wang, Z., Guo, S., Wehner, B., Nowak, A., Achtert, P., Wiedensohler, A., Jung, J., Kim, Y.J., 2009. Characteristics of aerosol size distributions and new particle formation in the summer in Beijing. *J. Geophys. Res.* Atmos. 114, D00G12. <http://dx.doi.org/10.1029/2008JD010894>.
- Yue, D.L., Hu, M., Zhang, R.Y., Wang, Z.B., Zheng, J., Wu, Z.J., Wiedensohler, A., He, L.Y., Huang, X.F., Zhu, T., 2010. The roles of sulfuric acid in new particle formation and growth in the mega-city of Beijing. *Atmos. Chem. Phys.* 10, 4953–4960. <http://dx.doi.org/10.5194/acp-10-4953-2010>.
- Zhang, Y., Obrist, D., Zielinska, B., Gertler, A., 2013. Particulate emissions from different types of biomass burning. *Atmos. Environ.* 72, 27–35. <http://dx.doi.org/10.1016/j.atmosenv.2013.02.026>.
- Zhang, S.L., Ma, N., Kecorius, S., Wang, P.C., Hu, M., Wang, Z.B., Größl, J., Wu, Z.J., Wiedensohler, A., 2016. Mixing state of atmospheric particles over the North China Plain. *Atmos. Environ.* 125, 152–164.
- Zheng, X., Liu, X., Zhao, F., Duan, F., Yu, T., Cachier, H., 2005. Seasonal characteristics of biomass burning contribution to Beijing aerosol. *Sci. China Ser. B Chem.* 48 (5), 481–488.
- Zhuang, B.L., Li, S., Wang, T.J., Deng, J.J., Xie, M., Yin, C.Q., Zhu, J.L., 2013. Direct radiative forcing and climate effects of anthropogenic aerosols with different mixing states over China. *Atmos. Environ.* 79, 349–361.